Laser-Beam-Patterned Topological Insulating States on Thin Semiconducting MoS_2

H. Mine,[1] A. Kobayashi,[1] T. Nakamura,[2] T. Inoue,[3] S. Pakdel,[5,6,9] D. Marian,[7] E. Gonzalez-Marin,[7] S. Maruyama,[3] S. Katsumoto,[2] A. Fortunelli,[8] J. J. Palacios,[4,5] and J. Haruyama[1,2,*]

[1]*Faculty of Science and Engineering, Aoyama Gakuin University, 5-10-1 Fuchinobe, Sagamihara, Kanagawa 252-5258, Japan*
[2]*Institute for Solid State Physics, The University of Tokyo, 5-1-5 Kashiwanoha, Kashiwa, Chiba 277-8581, Japan*
[3]*Department of Mechanical Engineering, The University of Tokyo, 7-3-1 Hongo, Bunkyo-ku, Tokyo 113-8656, Japan*
[4]*Department of Physics, The University of Texas at Austin, Austin, Texas 78712, USA*
[5]*Departamento de Física de la Materia Condensada, Instituto Nicolás Cabrera (INC), and Condensed Matter Physics Center (IFIMAC), Universidad Autónoma de Madrid, E-28049 Madrid, Spain*
[6]*School of Electrical and Computer Engineering, University College of Engineering, University of Tehran, Tehran 14395-515, Iran*
[7]*Dipartimento di Ingegneria dell'Informazione, Università di Pisa, Pisa 56122, Italy*
[8]*CNR, National Research Council, Pisa 56124, Italy*
[9]*Department of Physics and Astronomy, Aarhus University, 8000 Aarhus C, Denmark*

(Received 4 November 2018; revised manuscript received 3 July 2019; published 2 October 2019)

Identifying the two-dimensional (2D) topological insulating (TI) state in new materials and its control are crucial aspects towards the development of voltage-controlled spintronic devices with low-power dissipation. Members of the 2D transition metal dichalcogenides have been recently predicted and experimentally reported as a new class of 2D TI materials, but in most cases edge conduction seems fragile and limited to the monolayer phase fabricated on specified substrates. Here, we realize the controlled patterning of the $1T'$ phase embedded into the $2H$ phase of thin semiconducting molybdenum-disulfide by laser beam irradiation. Integer fractions of the quantum of resistance, the dependence on laser-irradiation conditions, magnetic field, and temperature, as well as the bulk gap observation by scanning tunneling spectroscopy and theoretical calculations indicate the presence of the quantum spin Hall phase in our patterned $1T'$ phases.

DOI: 10.1103/PhysRevLett.123.146803

Two-dimensional (2D) topological insulting (TI) states have been mainly investigated in HgTe/CdTe or InAs/GaSb quantum well systems [1–3]. In the 2D TI state, the quantum spin Hall effect (QSHE) emerges thanks to the simultaneous presence of a bulk energy gap and gapless helical edge states protected by time-reversal symmetry, namely, opposite and counterpropagating spin states forming a Kramers doublet. Interestingly, 2D TI states were first theoretically predicted for graphene [4–6], but experimentally reported in only few related systems [7–9] such as low-coverage Bi_2Te_3-nanoparticle-decorated graphene [8]. Moreover, control of the quantum spin Hall (QSH) phase in graphene-based systems remains a challenge.

Recently, a family of atom-thin transition metal dichalcogenides (TMDCs) has also been predicted to exhibit the QSHE [10–12], having its origin in the natural band inversion of the $1T'$ phase (one of the phases of TMDC; see Supplementary Material, Sec. I [13]) and the spin-orbit coupling (SOC)-induced band gap opening. Moreover, the TI state has been experimentally verified in the case of WTe_2 [25–27] thanks to the stability and high-quality of WTe_2 monolayers carefully formed on a hybrid substrate of bilayer graphene and monolayer hexagonal boron nitride. Various signatures of the TI state have been demonstrated in this material [25,27], including the latest observation of a half-integer quantum value of resistance ($R_Q/2 = h/2e^2 = 12.9$ kW, where h is Planck's constant and e is the charge on the electron) [26].

However, the TI phenomenon in WTe_2 is rather sensitive to the substrates, synthesis process, and the chemical environment, making its controlled use in practical applications challenging. Moreover, although the (metastable) $1T'$ phase can be found or induced in other TMDCs [28,29], nobody has demonstrated the existence of the QSHE in these other TMDCs except for [30]. The conditions under which helical edge states can exist at the $1T'$-$2H$ interfaces is a crucial problem that should be mastered for both TI physics and its applications. Here, we pattern a metallic $1T'$ phase (Supplemental Material, Sec. I [13]) embedded into the nontopological and semiconducting $2H$ phase of thin molybdenum-disulfide (MoS_2) flakes, one of the TMDC family, via a facile protocol based on laser beam irradiation [28] and, via transport measurements, reveal that the embedded $1T'$ phase exhibits the TI state.

In the present experiments, thin MoS_2 flakes are obtained by mechanical exfoliation of the bulk material

and transferred onto a SiO_2/Si substrate. Layer thicknesses of ~17 nm have been confirmed by atomic force microscopy (AFM) and optical microscopy (OM). OM and AFM images of a flake with two different patterns created by laser beam irradiation are shown in Figs. 1(a) and 1(b) (Supplemental Material, Sec. II [13]). The large rectangular pattern (with two electrode probes) is analogous to that previously used for graphene under high magnetic fields [9] and for monolayer WTe_2 [26]. In contrast, the H-letterlike pattern is analogous to that used in HgTe/CdTe quantum wells [1] and in our previous Bi_2Te_3-nanoparticle-decorated graphene system [8]. The presence of helical edge states was confirmed in all these systems. In the OM image, the color of the irradiated patterns drastically changes to semitransparent [Fig. 1(a)]. The cross-sectional AFM image of the irradiated part reveals a decrease in the thickness of about 10 nm [Fig. 1(b)]. These observations are consistent with previous reports in multilayer $MoTe_2$ [28], which demonstrated a layer thinning effect caused by the burnout of individual monolayers due to in plane heat accumulation from the laser beam irradiation. Heat introduced by the laser irradiation causes, in turn, a $2H$-$1T'$ transition in the upper layers [Fig. 1(c)] [28] (Supplemental Material, Sec. III [13]).

Typical Raman spectra are shown in Fig. 1(d) and we can use them to estimate the number of $1T'$ layers formed. For the nonlaser-irradiated region ($2H$ phase), the Raman peaks are evident for multilayer (>5 layers) MoS_2, showing the large and characteristic E_{2g} and A_{1g} peaks, while the pattern of the peaks for the laser-irradiated region ($1T' + 2H$) has definitely changed. Both peaks are still visible, which can be attributed to the $2H$ layers remaining underneath the $1T'$ layers (Supplemental Material, Sec. III [13]), while the other peaks can be certainly attributed to the $1T'$ phase [31].

Photoluminescence (PL) signals of the laser-irradiated parts are shown in Figs. 1(e) and 1(f) reveal that the peak positions shifted to lower wavelengths (i.e., higher energies) and the peak intensities decreased with laser-irradiation time. This is also compatible with the above-mentioned interpretation. When the upper layers are transformed into the $1T'$ phase, these layers cause no PL signals [32], while the remaining bottom semiconducting layers still yield a (reduced) signal [Fig. 1(c)]. Furthermore, x-ray photoelectron spectroscopy (XPS) of the laser-irradiated part demonstrates the two types of hybridization of Mo 3d orbitals associated with the $1T'$ and $2H$ phases [Fig. 1(g)].

Resistance (R) measurements as a function of back gate voltage (V_{BG}) of the samples shown in Fig. 1(a) are shown in Fig. 2. Au/Ti electrodes are in contact only with four corners of the rectangular pattern and each branch of the H-letterlike pattern so as to measure charge-spin transport only in the $1T'$ region [insets of Figs. 2(a) and 2(c)].

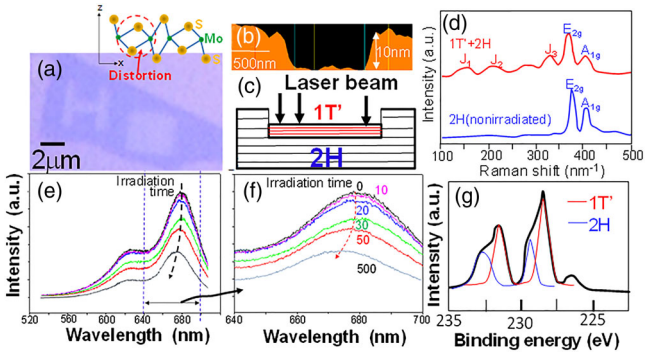

FIG. 1. (a) Optical microscopy image of the $1T'$ phase rectangular (right) and H-letterlike (left) patterns formed onto a thin $2H$-MoS_2 flake by laser beam irradiation. (Inset) Schematic cross section of a crystal structure of $1T'$-MoS_2 monolayer with distortion. (b) AFM image of a cross section of the laser irradiated part. (c) Schematic cross section of $1T'$ phase part created by laser beam irradiation onto few-layer MoS_2, corresponding to (b). (d) Raman spectra for nonlaser-irradiated region ($2H$ phase; blue curve) and irradiated region ($1T'$ phase on $2H$ phase; red curve). Individual peaks correspond to $E_{2g} \sim 382$ nm^{-1} and $A_{1g} \sim 408$ nm^{-1} for $2H$ phase, $J_1 \sim 155$, $J_2 \sim 225$, and $J_3 \sim 330$ nm^{-1} for $1T'$ phase. (e),(f) PL spectra of the laser beam irradiated points plotted for wavelengths (e) 530–710 and (f) 640–700 nm. The numbers on the graph are the irradiation time for each plotted line and are common to both (e) and (f). (g) XPS of the sample after laser irradiation. Red and blue lines are data fits for spectra of the $1T'$ and $2H$ phases, respectively.

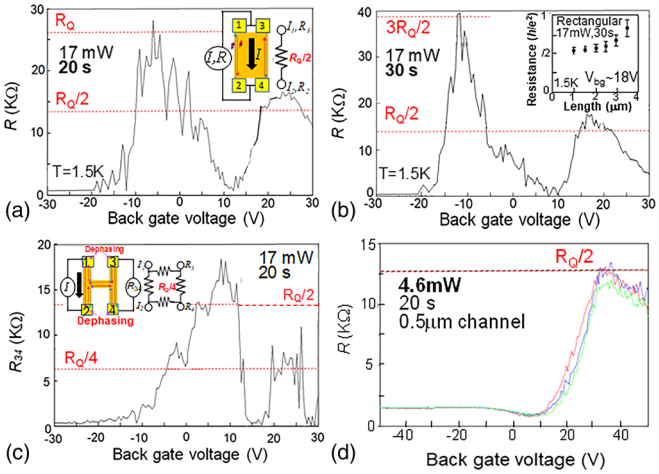

FIG. 2. (a),(b) For the $1T'$ rectangular patterns formed by two different laser irradiation times on each point; two-terminal resistance measured between electrode pairs 1,3 and 2,4 as a function of V_{BG} by flowing a constant current between electrode pairs 1,3 and 2,4 (insets). Contact resistances with $1T'$ metallic-layer resistances are subtracted. (c) For the $1T'$ H-letterlike pattern: nonlocal resistance (R_{NL}) observed for electrode pairs 3-4 as a function of V_{BG}, when a constant current flows between electrode pairs 1-2 (inset). (d) For the $1T'$ rectangular pattern formed by reduced laser power, with a short channel. Three different colors correspond to three different measurements. Equivalent circuits are shown in insets of (a) and (b). (b, inset) Channel length dependence of R peak values in high V_{BG} regions. Error bars are for the results of each of the three samples.

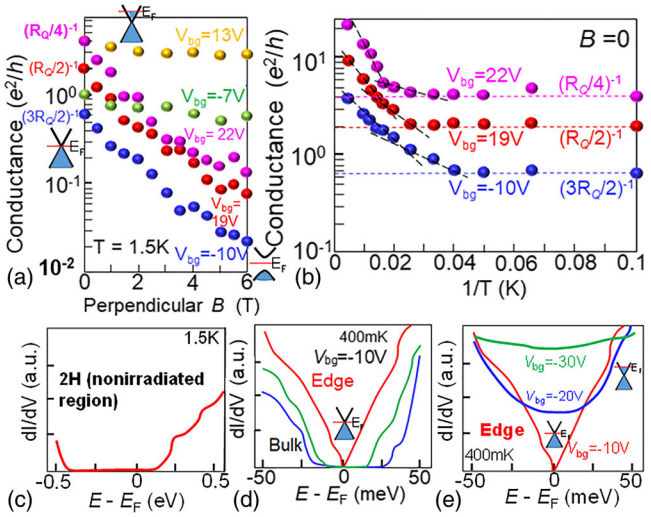

FIG. 3. (a) Out-of-plane magnetic-field ($B_\perp$) dependence of conductance corresponding to inverse of the three R peaks [blue and red symbols for Fig. 2(b) (rectangular pattern) and pink for high V_{BG} of Fig. 2(c) (H-letterlike pattern)] and two off-R peak values [green and orange symbols for Fig. 2(b)]. (b) Temperature dependence of conductance corresponding to the three R peaks in (a) in Arrhenius plot format. Dashed lines are guides to the eyes. (c)–(e) STS spectra for nonlaser-irradiated $2H$ region (c) and irradiated $1T'$ region (d),(e) (Supplemental Material, Sec. IX [13]). (d) The two bulk signals (blue and green lines) were measured near the center of the $1T'$ rectangular pattern, and the edge signal (red line) was measured near the boundary of the $1T'/2H$ phases. (e) The edge signals for different three V_{BG} values in sample of (d). The $1T'$ region was formed by irradiation with the condition for Fig. 2(b). (Insets) Schematic views of band diagram near or away from Kramers degeneracy point with Fermi level (E_F).

Because of the presence of a Schottky barrier at the $1T'/2H$ junction [$> \sim 0.2$ eV; see Fig. 3(c) for the semiconducting band gap in the $2H$ region] [32,33], the $2H$ semiconducting layers below the $1T'$ layers are expected to give a negligible contribution to these measurements, particularly at low temperatures.

For the rectangular pattern, the two-terminal resistance between electrodes 1 and 3 and electrodes 2 and 4 is measured as a function of V_{BG} by flowing a constant current between electrodes 1 and 3 and electrodes 2 and 4 (see insets). The results of two samples formed using different irradiation times (20 and 30 s) are shown in Figs. 2(a) and 2(b), respectively. Individual figures demonstrate two R peaks (Supplemental Material, Sec. X [13]). At high V_{BG}, R peaks of $R_{34} \approx R_Q/2$ are confirmed in both figures [at $V_{BG} \approx +25$ and $+19$ V in Figs. 2(a) and 2(b), respectively]. Larger R peaks are also observed at negative V_{BG}'s [$R_{34} \approx R_Q$ and $\approx 3R_Q/2$ at $V_{BG} \approx -5$ and ≈ -10 V in Figs. 2(a) and 2(b), respectively]. For the H-letterlike pattern, when a constant current flows between electrode pair 1-2, the nonlocal resistance (R_{NL}) between electrode pair 3-4 (R_{34}) is measured as a function of V_{BG} [see inset of Fig. 2(c)]. Figure 2(c) shows the result. An R_{NL} plateau of $R_{34} \approx R_Q/4$ at high $V_{BG}(\approx +20$–25 V) is confirmed with an R_{NL} peak of $R_{34} > R_Q/2$ at low $V_{BG}(\approx +5$ V) also appearing. As usually occurs, large V_{BG} values need to be applied to significantly tune the Fermi level via the SiO_2/Si substrate [34] (Supplemental Material, Sec. IV [13]).

The $R_Q/2$ and $R_Q/4$ of R peak values observed at high V_{BG} suggests the appearance of the QSH phase without and with dephasing in metal electrodes, respectively [1,8]. First, the R peak values $\sim R_Q/2$ confirmed for the $1T'$ rectangular patterns [Figs. 2(a) and 2(b)] are consistent with the presence of helical edge modes without dephasing. In this case, the two counterpropagating spin channels can be preserved at two different quasichemical potentials between the electrodes, leading to a net current flow along the edges with R equal to $R_Q/2$ (as based on the Landauer-Büttiker formalism). Such a two-terminal resistance plateau $\sim R_Q/2$, reported in both rectangular monolayer WTe_2 [26] and in large rectangular graphene under high magnetic fields with a similar electrode connection to the present one [insets of Figs. 2(a) and 2(b)] [9], was presented as evidence for helical edge states [35]. Wu *et al.*[26] also reported deviations from $\sim R_Q/2$ to larger values in long-channel samples ($\gg$a few 100 nm). Remarkably, in our case, R does not deviate significantly from $R_Q/2$, even for ~ 1 μm channel lengths, because of the possibly high uniformity of the $1T'$ phase formed by our highly uniform laser beam (Supplemental Material, Sec. V [13]).

Second, the R_{NL} plateau value $\sim R_Q/4$ [Fig. 2(c)] corresponds to the case of helical edge modes with dephasing in the metal electrodes in the H-letterlike pattern with four metal electrodes (inset) and nicely agrees with the result in Refs. [1,8]. Once the helical edge electrons enter the voltage electrodes, they interact with a reservoir containing an infinite number of low-energy degrees of freedom so that time-reversal symmetry is effectively broken by the macroscopic irreversibility. In particular, a resistance plateau can be confirmed in Fig. 2(c). The plateau shape, as opposed to a peak, is attributed to the channel width being narrower (~ 1 μm) than that in the rectangular pattern (~ 2 μm) and the usage of a highly uniform laser beam, as mentioned above (Supplemental Material, Sec. VI [13]). This is also consistent with the results in [1]. Consequently, the two counterpropagating channels equilibrate at the same chemical potential, determined by the voltage of the metallic electrodes, leading to dissipation and, thus, emergence of integer fractions of R_Q. Therefore, these R peaks (i.e., $\sim R_Q/2$ in the rectangular pattern and $\sim R_Q/4$ in the H-letterlike pattern) evidently suggest the presence of the helical edge states in the patterned $1T'$ layers [36].

Indeed, we observe a single R peak with an $R_Q/2$ value, which is consistent with a conventional QSH phase [26], when a lower-power laser is irradiated ($\sim$4.6 mW)

[Fig. 2(d)]. This supports the above-mentioned argument that the observed two R peaks with the large peak values [Figs. 2(a) and 2(c)] are attributed to the excess heat accumulation through the multilayers caused by the present high-power laser irradiation. The low-power laser irradiation suppresses the excess heat accumulation and allows a topological transition in monolayer with less edge defects (Supplemental Material, Sec. III [13]).

Perpendicular magnetic-field ($B_\perp$) dependence measurements for the samples shown in Figs. 2(b) and 2(c) are demonstrated in Fig. 3(a). As $B_\perp$ increases, the conductance G, corresponding to the inverse of three R peak values in Figs. 2(b) and 2(c), exponentially decreases. G values corresponding to the inverse of two off-R peaks [Fig. 2(b)] remain almost unchanged. These results are in good agreement with those in the QSHE observed in WTe_2 [26] and our Bi_2Te_3-decorated graphene [8] and evidently support the fact that the first three R peaks can be attributed to helical edge states. Only when the Fermi level is set to the Kramers degeneracy point, R values can well reflect the band gap opening due to the Zeeman effect caused by applied $B_\perp$ (see insets), resulting in the observed exponential decrease in G [37].

As far as zero-$B_\perp$ temperature dependence is concerned, G corresponding to the inverse of the three R peak values ($R_Q/2$, $3R_Q/2$, and $R_Q/4$) remain constant up to the transition temperatures (T_{c1}) of ~40 (red symbol), ~25 (blue), and ~30 K (pink), respectively [Fig. 3(b)]. At temperatures higher than the individual T_{c1}, G increases as temperature increases, following the thermal activation formula [i.e., a linear dependence in the Arrhenius plot of Fig. 3(b)] with activation energies of ~15 (red symbol), ~10 (blue), and ~7 meV (pink), respectively. Moreover, G increases again above $T_{c2} \sim 60$ (red), ~50 (blue), and ~60 K (pink), respectively, with larger slopes. The T_{c1}, which are lower than 100 K as reported in WTe_2 [26], are attributed to bulk gaps being smaller than that of WTe_2 [38]. In contrast, G increases at temperatures $> T_{c2}$ have not been observed previously [8,26]. This can be attributed to the thermally activated carriers flowing into the $1T'$ QSH phase region from the $2H$ semiconducting region over the Schottky barrier (or band discontinuity) at the $1T'/2H$ layer interface, because the barrier height is much larger than the bulk gaps [33]. The largest activation energy (i.e., barrier height or band discontinuity) for the pink symbol is consistent with the smallest gap value of ~7 meV as mentioned above.

Scanning tunneling spectroscopy (STS) spectra of the nonlaser-irradiated $2H$ region and the irradiated rectangular $1T'$ pattern are shown in Figs. 3(c) and 3(d,e), respectively (Supplemental Material, Sec. IX [13]). Figure 3(c) demonstrates evident gaps ~0.6 eV, which are in good agreement with the n-type semiconducting gap of thin MoS_2 with the number of the layers larger than 5. This gap is large enough to embed the present topological gaps with ~10 meV order. For Fig. 3(d) with V_{BG} tuned to the Kramers degeneracy point, in the two bulk points, STS gaps of ~25–35 meV are confirmed, while the gap disappears at an edge. The bulk gap values almost agree with the values estimated from the temperature dependence of resistance peaks, as mentioned above. Although they are smaller than the 45 meV gap reported in $1T'$-WTe_2 [27], they are appropriate for $1T'$-MoS_2. For Fig. 3(e), as V_{BG} runs away from the Kramers degeneracy point (i.e., $V_{BG} \sim -10$ V) (see insets), the dI/dV increases and the dI/dV dip disappears, resulting in just a metallic behavior of the $1T'$ phase. This supports the fact that the disappearance of the bulk gap in Fig. 3(d) is attributed to the edge current due to the Kramers degeneracy point. Consequently, all results suggest that the laser-created $1T'$ phases can be in QSH phases with helical edge modes.

The existence of helical edge states at the $1T'/2H$ interface is further supported by our theoretical calculations [39]. Figure 4(a) shows the overall band structure of the heterostructure. Our choice of a centrosymmetric system with two interfaces makes all the bands doubly degenerate. One can clearly identify the bulk band inversion associated with the $1T'$ phase near Γ and the gap opened by the SOC (enhanced by the quantum confinement due to the finite width of the $1T'$ region). Importantly, we learn from these calculations that the $1T'$ phase gap is in the middle of the

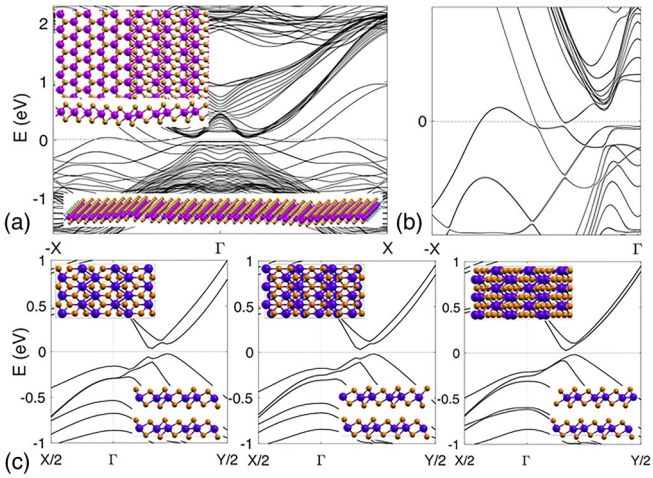

FIG. 4. (a) Overall band structure of the $2H/1T'/2H$ heterostructure. (Bottom inset) A view of the whole heterostructure showing the passivated edges. (Top inset) Atomic detail of one interface. The yellowish area indicates the energy window within the $2H$ phase gap. Inside this range and near the center of the Brillouin zone, the bulk band inversion of the $1T'$ phase and the gap opened by the SOC can be seen along with nontrivial and trivial bands. (b) Enlargement of the bands into the relevant energy window. The number of band crossings at the Fermi level (placed at zero) and at any energy in the gap is odd, as expected from the presence of protected interface states. (c) Bulk band structure of a bilayer for three different stacking possibilities (indicated in the insets), showing a gap in all of them.

much larger gap of the 2*H* phase, which should enable the manifestation of the protected helical states along the interfaces. Figure 4(b) shows an enlargement of the band structure in the relevant low-energy sector in half of the Brillouin zone. Despite the complexity of the band structure, which stems from the presence of native trivial edge states of the zigzag edges of the 2*H* phase [40], the total number of crossings at any energy within the gap in half of the Brillouin zone is odd, as expected.

Figure 4(c) shows the band structure of a bilayer for different stacking geometries (shown in the insets). These three geometries do not exhaust all stacking possibilities, but are representative of those found in bulk materials. After relaxation, a gap remains open in all cases [41], which is a necessary condition for the observation of the QSH phase. Also, the band structure reflects the weak coupling between layers, which also facilitates the observation of the QSH phase.

Controlled patterning of the 1T' phase onto the 2*H* phase of thin semiconducting MoS_2 by laser beam irradiation has been demonstrated. Using multilayers brings many advantages to the present laser beam irradiated experiments (e.g., protection from laser damage and oxidation) (Supplemental Material, Sec. 11 [13]). Further optimization of the conditions for laser irradiation will allow for on-demand patterning of 2D (or 1D) topological phases onto desired positions of nontopological phases of TMDCs and will facilitate the path towards topological quantum computation [42].

The authors thank S. Tang, Z.-X. Shen, A. MacDonald, S. Murakami, Y. Shimazaki, T. Yamamoto, S. Tarucha, T. Ando, R. Wu, J. Alicea, M. Dresselhaus, P. J.-Herrero, and P. Kim for their technical contributions, fruitful discussions, and encouragement. The work carried out at Aoyama Gakuin University was partly supported by a grant for private universities and a Grant-in-Aid for Scientific Research (JP15K13277) awarded by MEXT. The work at the University of Tokyo was partly supported by Grant-in-Aid for Scientific Research (JP17K05492, JP18H04218, and JP19H00652). J. J. P. and S. P. acknowledge Spanish MINECO through Grant No. FIS2016-80434-P, the Fundación Ramón Areces, the María de Maeztu Program for Units of Excellence in R&D (MDM-2014-0377), the Comunidad Autónoma de Madrid through NANOMAGCOST Program, and the European Union Seventh Framework Programme under Grant Agreement No. 604391 Graphene Flagship. S. P. acknowledges the computer resources and assistance provided by the Centro de Computación Científica of the Universidad Autónoma de Madrid. S. P. was also supported by the VILLUM FONDEN via the Center of Excellence for Dirac Materials (Grant No. 11744). D. M. and E. G.-M. gratefully acknowledge support from the Graphene Flagship Graphene Core2 Contract No. 785219. E. G.-M also acknowledges IJCI-2017-32297 from Spanish MINECO/AEI. D. M., E. G.-M., and A. F. are very grateful to Gianluca Fiori and Giuseppe Iannaccone for continuous support, strong encouragement, and enlightening discussions.

*To whom all correspondence should be addressed.
J-haru@ee.aoyama.ac.jp

[1] A. Roth, C. Brüne, H. Buhmann, L. W. Molenkamp, J. Maciejko, X.-L. Qi, and S.-C. Zhang, Science **325**, 294 (2009).
[2] C. Brüne, A. Roth, H. Buhmann, E. M. Hankiewicz, L. W. Molenkamp, J. Maciejko, X.-L. Qi, and S.-C. Zhang, Nat. Phys. **8**, 485 (2012).
[3] L. J. Du, I. Knez, G. Sullivan, and R.-R. Du, Phys. Rev. Lett. **114**, 096802 (2015).
[4] C. L. Kane and E. J. Mele, Phys. Rev. Lett. **95**, 226801 (2005).
[5] J. Hu, J. Alicea, R. Wu, and M. Franz, Phys. Rev. Lett. **109**, 266801 (2012).
[6] H. Jiang, Z. Qiao, H. Liu, J. Shi, and Q. Niu, Phys. Rev. Lett. **109**, 116803 (2012).
[7] T. Nanba, K. Tamura, K. Hatsuda, T. Nakamura, C. Ohata, S. Katsumoto, and J. Haruyama, Appl. Phys. Lett. **113**, 053106 (2018).
[8] K. Hatsuda, H. Mine, T. Nakamura, J. Li, R. Wu, S. Katsumoto, and J. Haruyama, Sci. Adv. **4**, eaau6915 (2018).
[9] A. F. Young, J. D. S.-Yamagishi, B. Hunt, S. H. Choi, K. Watanabe, T. Taniguchi, R. C. Ashoori, and P. J.-Herrero, Nature (London) **505**, 528 (2014).
[10] C. Liu, T. L. Hughes, X.-L. Qi, K. Wang, and S.-C. Zhang, Phys. Rev. Lett. **100**, 236601 (2008).
[11] X. Qian, J. Liu, L. Fu, and J. Li, Science **346**, 1344 (2014).
[12] L. Kou, Y. Ma, Z. Sun, T. Heine, and C. Chen, J. Phys. Chem. Lett. **8**, 1905 (2017).
[13] See Supplemental Material at http://link.aps.org/supplemental/10.1103/PhysRevLett.123.146803 for details of contents, fabrication, measurements, and calculation methods, which also includes Refs. [14–24].
[14] R. Dovesi, R. Orlando, A. Erba, C. M. Zicovich-Wilson, B. Civalleri, S. Casassa, L. Maschio, M. Ferrabone, M. De La Pierre, and P. D'Arco, Int. J. Quantum Chem. **114**, 1287 (2014).
[15] For program description, see http://www.crystal.unito.it/.
[16] R. Dovesi, V. Saunders, C. Roetti, R. Orlando, C. Zicovich-Wilson, F. Pascale, B. Civalleri, K. Doll, N. Harrison, and I. Bush, *CRYSTAL14 User's Manual* (University of Torino, Torino, Italy, 2018).
[17] S. Pakdel, M. Pourfath, and J. J. Palacios, J. Nanosci. Nanotechnol. **9**, 1015 (2018).
[18] Y.-C. Lin, D. O. Dumcenco, Y.-S. Huang, and K. Suenaga, Nat. Nanotechnol. **9**, 391 (2014).
[19] P. Giannozzi, S. Baroni, N. Bonini, M. Calandra, R. Car, C. Cavazzoni *et al.*, J. Phys. Condens. Matter **21**, 395502 (2009).
[20] J. P. Perdew, K. Burke, and M. Ernzerhof, Phys. Rev. Lett. **77**, 3865 (1996).

[21] G. Prandini, A. Marrazzo, I. E. Castelli, N. Mounet, and N. Marzari, npj Comput. Mater. **4**, 72 (2018); K. Lejaeghere *et al.*, Science **351**, aad3000 (2016); http://www.materialscloud.org/sssp.
[22] G. Kresse and J. Furthmüller, Comput. Mater. Sci. **6**, 15 (1996).
[23] G. Kresse and D. Joubert, Phys. Rev. B **59**, 1758 (1999).
[24] J. Heyd, G. E. Scuseria, and M. Ernzerhof, J. Chem. Phys. **118**, 8207 (2003).
[25] Z. Fei, T. Palomaki, S. Wu, W. Zhao, X. Cai, B. Sun, P. Nguyen, J. Finney, X. Xu, and D. H. Cobden, Nat. Phys. **13**, 677 (2017).
[26] S. Wu, V. Fatemi, Q. D. Gibson, K. Watanabe, T. Taniguchi, R. J. Cava, and P. J.-Herrero, Science **359**, 76 (2018).
[27] S. Tang *et al.*, Nat. Phys. **13**, 683 (2017).
[28] S. Cho *et al.*, Science **349**, 625 (2015).
[29] M. M. Ugeda *et al.*, Nat. Commun. **9**, 3401 (2018).
[30] H. Xu, D. Han, Y. Bao, F. Cheng, Z. Ding, S. J. R. Tan, and K. P. Loh, Nano Lett. **18**, 5085 (2018).
[31] Because the thickness of the laser-irradiated part is ∼7 nm and the minimum thickness expected for the remaining $2H$ layers underneath the $1T'$ ones is 5 layers × ∼0.7 nm = ∼3.5 nm (the minimum thickness to get the Raman signal), we estimate a maximum thickness for the $1T'$ layers of ∼3.5 nm. Since we expect the laser irradiation to slightly damage the topmost $1T'$ layers, the number of pristine $1T'$ layers is expected to be at most a few.
[32] Y. Yu *et al.*, Nat. Chem. **10**, 638 (2018).
[33] Y. Katagiri, T. Nakamura, A. Ishii, C. Ohata, M. Hasegawa, S. Katsumoto, T. Cusati, A. Fortunelli, G. Iannaccone, G. Fiori, S. Roche, and J. Haruyama, Nano Lett. **16**, 3788 (2016).
[34] T. Shimizu, J. Haruyama, D. C. Marcano, D. V. Kosinkin, J. M. Tour, K. Hirose, and K. Suenaga, Nat. Nanotechnol. **6**, 45 (2011).
[35] It should be noted that the R peak values $\sim R_Q/2$ observed in Figs. 2(a) and 2(b) are slightly larger than $R_Q/2$ (~ 0.55–$0.6R_Q$). This deviation agrees well with the R plateau value of $0.56R_Q$ observed in Ref. [9], attributed to the microscopic details of the edges (e.g., local charge puddles) [3,8]; S. Essert and K. Richter, 2D Mater. **2**, 024005 (2015). Indeed, a somewhat irregular boundary (i.e., topological and nontopological phase junction) can be observed at some points of our $1T'/2H$ junction at the topmost surface layer (Supplemental Material, Sec. VII), which is noticeably different from clean interfaces of other parts and may lead to local charge puddles.
[36] These R peaks without influence of dephasing will originate from either monolayer or a few layers existing below the top-surface layer, while it is speculated that the other R peaks [$\sim R_Q$ and $\sim 3R_Q/2$ in Figs. 2(a) and 2(b), respectively], which are typically larger than those observed at high V_{BG}, are derived from the top-surface $1T'$ layer with edge defects (Supplemental Material, Secs. 7 and 8 [13]). The top-surface layer has multiple defects introduced by the high-power (i.e., ∼17 mW) laser irradiation and presumably presents a different stoichiometry (a Kramers degeneracy point different from other layers) and conductivity properties, including more defects along the edges of the $1T'/2H$ interface (Supplemental Material, Sec. VII [13]), which can act as dephasing centers. This layer may be weakly coupled to the pristine $1T'$ layer(s) existing underneath, due to an excess in plane heat accumulation (Supplemental Material, Secs. 7 and 8 [13]).
[37] The pink symbol observed in the H-letterlike pattern shows a saturation at lower $B_\perp$ (∼3 T), because the channel width (∼1 μm) is smaller than the rectangular pattern and other edge effects may disturb the exponential G decrease.
[38] Three possible origins are considered for the deviation from $(R_Q/2)^{-1}$, $(R_Q/4)^{-1}$, and $(3R_Q/2)^{-1}$ at $T > T_{c1}$: (1) thermally activated spins over the bulk gap, (2) spin fluctuation in helical edge spins, and (3) induced dephasing in metal electrodes. The approximate agreement with the STS gaps suggests that (1) is dominant, consistent with the fact that the activation energy observed at $B = 0$ can correspond to the bulk gap.
[39] We first examine the electronic states of a heterostructure formed by two interfaces dividing a $2H$ MoS_2 monolayer into three regions, $2H/1T'/2H$ [see inset in Fig. 4(a)]. The three regions are infinite along the interfaces direction, but the system is finite along the perpendicular one. The relaxed atomic positions of the unit cells near the interfaces [detail shown in Fig. 4(b)] are obtained from density-functional theory (DFT) structural relaxations, in which we have kept a flat structure away from the interfaces to simulate the underlying MoS_2 layers. We have corroborated our modeling by investigating other atomistic models of the $2H/1T'$ interface, starting from different initial configurations, also considering an asymmetric periodic model, and relaxing them using different constraints (see Supplemental Material, Secs. 12 and 13 [13], which include Refs. [14–24]). The DFT results in all these investigated cases converged to a qualitatively similar picture in terms of structural stability and band structure, which supports the robustness of the model here proposed.
[40] W. S. Paz and J. J. Palacios, 2D Mater. **4**, 015014 (2016).
[41] Following F. Zheng *et al.*, Adv. Mater. **28**, 4845 (2016), and given the semimetallic character of the bilayers, the use of a hybrid functional is advised in these calculations. We have employed VASP with HSE06 functionals to this aim (Supplemental Material, Sec. 12).
[42] V. Mourik, K. Zuo, S. M. Frolov, S. R. Plissard, E. P. A. M. Bakkers, and L. P. Kouwenhoven, Science **336**, 1003 (2012); M. T. Deng, S. Vaitiekėnas, E. B. Hansen, J. Danon, M. Leijnse, K. Flensberg, J. Nygård, P. Krogstrup, and C. M. Marcus, Science **354**, 1557 (2016).